



HAL
open science

Pulsed production of antihydrogen

Claude Amsler, Massimiliano Antonello, Alexander Belov, Germano Bonomi, Roberto Sennen Brusa, Massimo Caccia, Antoine Camper, Ruggero Caravita, Fabrizio Castelli, Patrick Cheinet, et al.

► **To cite this version:**

Claude Amsler, Massimiliano Antonello, Alexander Belov, Germano Bonomi, Roberto Sennen Brusa, et al. Pulsed production of antihydrogen. *Communications Physics*, 2021, 4 (1), pp.19. 10.1038/s42005-020-00494-z . hal-03150578

HAL Id: hal-03150578

<https://hal.science/hal-03150578>

Submitted on 24 Feb 2021

HAL is a multi-disciplinary open access archive for the deposit and dissemination of scientific research documents, whether they are published or not. The documents may come from teaching and research institutions in France or abroad, or from public or private research centers.

L'archive ouverte pluridisciplinaire **HAL**, est destinée au dépôt et à la diffusion de documents scientifiques de niveau recherche, publiés ou non, émanant des établissements d'enseignement et de recherche français ou étrangers, des laboratoires publics ou privés.

Pulsed production of antihydrogen

Claude Amsler¹, Massimiliano Antonello^{2,3}, Alexander Belov⁴, Germano Bonomi^{5,6}, Roberto Sennen Brusa^{7,8}, Massimo Caccia^{2,3}, Antoine Camper⁹, Ruggero Caravita^{8,9}, Fabrizio Castelli^{3,10}, Patrick Cheinet¹¹, Daniel Comparat¹¹, Giovanni Consolati^{3,12}, Andrea Demetrio¹³, Lea Di Noto^{14,15}, Michael Doser⁹, Mattia Fani^{9,14,15}, Rafael Ferragut^{3,16}, Julian Fesel⁹, Sebastian Gerber⁹, Marco Giammarchi³, Angela Gligorova¹, Lisa Theresa Glöggler⁹, Francesco Guatieri^{7,8}, Stefan Haider⁹, Alexander Hinterberger⁹, Alban Kellerbauer¹⁷, Olga Khalidova⁹, Daniel Krasnický¹⁵, Vittorio Lagomarsino¹⁵, Chloé Malbrunot⁹, Sebastiano Mariazzi^{7,8}, Viktor Matveev⁴, Simon Müller¹³, Giancarlo Nebbia¹⁸, Patrick Nedelec¹⁹, Lilian Nowak⁹, Markus Oberthaler¹³, Emmanuel Oswald⁹, Davide Pagano^{5,6}, Luca Penasa^{7,8}, Vojtech Petracek²⁰, Luca Povolo^{7,8}, Francesco Prelez³, Marco Prevedelli²¹, Benjamin Rienäcker⁹, Ole Røhne²², Alberto Rotondi^{6,23}, Heidi Sandaker²², Romualdo Santoro^{2,3}, Gemma Testera¹⁵, Ingmari Tietje⁹, Valerio Toso^{3,16}, Tim Wolz⁹, Pauline Yzombard^{17,26}, Christian Zimmer^{9,22,24} & Nicola Zurlo^{6,25}

Antihydrogen atoms with K or sub-K temperature are a powerful tool to precisely probe the validity of fundamental physics laws and the design of highly sensitive experiments needs antihydrogen with controllable and well defined conditions. We present here experimental results on the production of antihydrogen in a pulsed mode in which the time when 90% of the atoms are produced is known with an uncertainty of ~250 ns. The pulsed source is generated by the charge-exchange reaction between Rydberg positronium atoms—produced via the injection of a pulsed positron beam into a nanochanneled Si target, and excited by laser pulses—and antiprotons, trapped, cooled and manipulated in electromagnetic traps. The pulsed production enables the control of the antihydrogen temperature, the tunability of the Rydberg states, their de-excitation by pulsed lasers and the manipulation through electric field gradients. The production of pulsed antihydrogen is a major landmark in the AEGIS experiment to perform direct measurements of the validity of the Weak Equivalence Principle for antimatter.

The question of whether antimatter falls in the Earth's gravitational field with the same acceleration g as ordinary matter does not yet have a direct experimental answer, although indirect arguments constrain possible differences to below $10^{-6}g^{1-3}$. The universality of free fall (Weak Equivalence Principle—WEP) is the pillar of General Relativity that describes the gravitational force through a non-quantum field theory. The WEP has been directly verified with accuracy reaching 10^{-14} , but exclusively for matter systems⁴; nevertheless, General Relativity predicts the same gravitational behavior of matter and antimatter systems. The other fundamental interactions of nature, described by a relativistic quantum field theory—the Standard Model of particle physics—also show complete symmetry between matter and antimatter systems as a consequence of the CPT (Charge, Parity, Time reversal) theorem. This CPT symmetry demands, in particular, that bound states of antimatter should have the same energy levels and lifetimes as the corresponding matter systems. So far, no CPT or WEP violations have been observed in any physical system⁵. Experimental searches for possible violations of these principles with continuously increasing sensitivity provide constraints to extended and unified models⁶ of all the fundamental interactions, as well as to cosmology⁷, and, most significantly, they probe the foundations of our way of describing nature. In fact, in relativistic quantum field theories, the CPT symmetry is a consequence of only a few basic hypotheses (Lorentz invariance, locality, and unitarity⁸) and it is not related to details of specific models. The WEP is the foundation for General Relativity, and more generally, for all metric theories of gravity.

Antihydrogen (\bar{H}), the bound state of an antiproton (\bar{p}) and a positron (e^+), is a privileged antimatter system, as it is the unique stable bound state of pure antimatter that presently can be synthesized in laboratories. Its practically infinite intrinsic lifetime offers the possibility to realize experiments searching for tiny violations of CPT and of the WEP for antimatter with extremely high sensitivity. Spectroscopic measurements with long observation times benefit from the natural lifetime of about 1/8 s of the 1S–2S transition of H, corresponding to a relative linewidth of 10^{-15} , and thus in principle allowing CPT tests with comparable, or even higher, accuracies. In addition, very cold \bar{H} atoms—with sub-kelvin temperature—are one of the favored systems to test the validity of the WEP on antimatter through free fall experiments.

The first production of low-energy antihydrogen in Rydberg states, \bar{H}^* , by means of 3-body recombination of clouds of \bar{p} and e^+ ($\bar{p} + e^+ + e^+ \rightarrow \bar{H}^* + e^+$) mixed inside electromagnetic traps, dates back to 2002^{9,10}. Since then, \bar{H} progress has been steady: experiments trapping it have been performed¹¹, the comparison between the measured 1S–2S transition of magnetically trapped \bar{H} with that calculated for H in the same magnetic field has already provided a CPT test with 2×10^{-12} accuracy¹², the hyperfine splitting of the fundamental states of \bar{H} has been measured to be consistent with that of H with an accuracy of 4×10^{-413} , and an experimental bound on the \bar{H} electrical charge, Q_e (in which e is the elementary charge), of $|Q| < 0.71$ parts per billion has been established¹⁴. Different projects aiming at a direct measurement of g on antihydrogen are under way^{15–17} to improve on the result of the first direct attempt reported in ref. 16 and complementary to the parallel efforts in progress with other atomic systems containing antimatter^{18,19}.

While ordinary atoms are available in the laboratory in large numbers, working with antimatter requires dealing with very few anti-atoms. The development of sources of \bar{H} with controllable and tunable conditions (temperature, production time, Rydberg state) is highly relevant for new measurements or to further improve the accuracy and precision of already measured \bar{H} properties.

In particular, knowing the time of \bar{H} formation with such accuracy opens the possibility of efficient and immediate manipulation of the formed anti-atoms through lasers and/or pulsed electric fields for subsequent precision measurements.

Previous experimentally demonstrated schemes of \bar{H} production did not allow tagging the time of the formation with accuracy. The 3-body recombination²⁰ results in a quasi-continuous \bar{H} source, and while the charge exchange process used in ref. 21 provides in principle the possibility of some temporal tagging, the attained uncertainty on the time of formation of \bar{H} lie in the few hundreds of μ s range. In fact, in ref. 21 Rydberg positronium (Ps^*) is generated through the interaction of trapped e^+ with a beam of Cs atoms—slightly above room temperature—excited to Rydberg states with a pulsed laser at few cm from the e^+ , before flying through them. Ps^* then diffuse outwards to reach a stationary \bar{p} cloud. The \bar{H} formation time uncertainty is thus set by the spread of the velocity of the heavy Cs atoms in ref. 21.

A more accurate time definition—in principle reaching the ns scale—could potentially be reached through laser stimulated

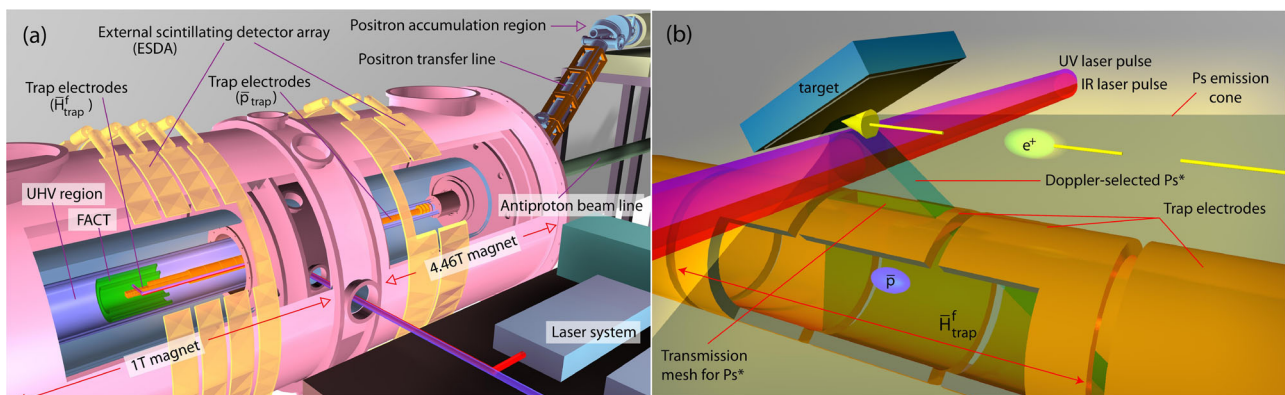


Fig. 1 Sketch of the AEGIS apparatus. **a** e^+ accumulation region on the top of the \bar{p} beam line and the e^+ transfer line (made of 0.1 T pulsed magnets) coupled to the cryostat of the superconducting magnets containing the \bar{p}_{trap} and \bar{H}_{trap}^f traps. The z-axis is the direction of the superconducting magnetic field. Also shown are the fast cryogenic tracker (FACT) detector and the external scintillating detector array (ESDA) surrounding the cryostat. The whole trap structure is made of 101 electrodes of various lengths, mounted inside the cryostat of the magnet, at a temperature of 10 K. **b** Blow-up of the \bar{H} production region. The \bar{H}_{trap}^f trap is located 1.3 cm below the target acting as e^+ to Ps converter and it features a special design with semi-transparent electrodes on top to allow the passage of Ps^* .

radiative recombination of mixed \bar{p} and e^+ clouds²². However, an experimental implementation has yet to be attempted.

We show in this paper the experimental results about production of \bar{H} in a pulsed mode in which the distribution of the time when \bar{H} are produced, with respect to a known reference time that triggers the formation process, features a full-width at half-maximum (FWHM) of 80 ns with 90% of the \bar{H} formed within 250 ns. This experimental determination of the \bar{H} production time is three orders of magnitude more accurate than previously attained.

Results

Charge exchange between \bar{p} and laser-excited positronium. The results described here have been obtained with the AEGIS (Antimatter Experiment: gravity, Spectroscopy, Interferometry)¹⁵ apparatus—shown in Fig. 1a, b—in operation at the CERN antiproton decelerator (AD)²³ with the primary goal of performing a direct measurement of g with a beam of cold anti-hydrogen using a classical moiré deflectometer²⁴. The pulsed formation is achieved through the charge exchange reaction^{25–27}



between trapped and cooled \bar{p} and positronium (Ps) in excited states (Ps^*). Bursts of $\sim 2 \times 10^6$ e^+ , with a FWHM lower than 10 ns, are accelerated to 4.6 keV and implanted into a nanochanneled silicon target²⁸ mounted above a region where cold antiprotons (~ 400 K) are confined by the electric and magnetic fields that form a Malmberg–Penning trap^{29,30} (\bar{H}_{trap}^f , see Fig. 1b). A fraction ($7.0 \pm 2.5\%$) of e^{+31} is emitted back from the target into the vacuum as ortho-Ps with a velocity distribution with the most probable value $\sim 10^5$ m s^{-132} . The emerging Ps is excited, in the 1 T magnetic field, to a manifold of Rydberg sublevels (Ps^*) distributed in energy around that of the $n_{\text{Ps}} = 17$ level that would have been reached in the absence of a magnetic field. The excitation is achieved through a sequence of two laser pulses³³, with wavelengths $\lambda_1 = 205.045$ nm (ultraviolet (UV) pulse) and $\lambda_2 = 1693$ nm (infrared (IR) pulse). The resulting Ps^* reaches the few mm-sized \bar{p} cloud, where it can lead to the formation of antihydrogen, on sub- μs timescales. The time of \bar{H} production is defined by the laser firing time (known with few ns accuracy) and the transit time of Ps^* toward the \bar{p} cloud. The measured distribution of the velocity of Ps^* in our apparatus³² and the cross-section reported in refs. 26,27 imply that the corresponding distribution of the \bar{H} formation time has a FWHM of ~ 80 ns, with an asymmetric tail due to the slowest Ps^* , resulting in 90% of the \bar{H} being produced within an ~ 250 -ns-wide time window.

\bar{H} is not trapped in our apparatus so that, after production, it drifts outwards until it annihilates on the surrounding material, producing pions, from \bar{p} annihilation, and γ , from the e^+ annihilation. The evidence of formation of \bar{H} is obtained by detecting, in a time window around the laser firing time, the signals originating from the pions in an external scintillating detector array (called here ESDA) read out by photomultipliers (PMTs). A cold \bar{p} plasma is prepared in ~ 1000 s and kept trapped in the \bar{H}_{trap}^f , the region in which \bar{H} will be formed, while several bursts (up to 80, typically 20–30) of e^+ are successively implanted in the silicon target—one burst every 130 s—until the \bar{p} plasma is dumped from the trap and a new one is reloaded. We call \bar{H}_{cycle} each single e^+ implantation. The analysis is based on 2206 \bar{H}_{cycle} with on average 5×10^5 \bar{p} and 2×10^6 e^+ in each cycle. We observed 79 events in the signal region, while we expect to detect 33.4 ± 4.6 events under the hypothesis of absence of \bar{p} formation. From this comparison, we reject the null hypothesis with 4.8 σ (local significance).

The number of produced \bar{H} is consistent with that expected from a dedicated Monte Carlo simulation accounting for the number of available \bar{p} and Ps^* and all the relevant physical and geometrical parameters.

The agreement between the observed and expected number of \bar{H} allows predicting that a significantly larger (by some orders of magnitude) flux of anti-atoms will be available in an optimized experimental geometry and with an increased number of \bar{p} and e^+ .

Experimental conditions and apparatus. The pulsed formation of \bar{H} through the charge exchange reaction and its detection in our apparatus requires the preparation of two ingredients: a sample of trapped cold antiprotons and a pulsed source of cold Ps^* . The values of the Ps^* and \bar{p} velocities in the laboratory frame are in principle not relevant for establishing an efficient \bar{H} production through charge exchange. Only a low relative velocity v_r between Ps^* and \bar{p} in fact matters because the cross-section abruptly drops if v_r is well above the velocity of e^+ in the classical Ps orbit²⁶. This means that we need $v_r < 1.3 \times 10^5$ m s^{-1} if the Ps principal quantum number is $n_{\text{Ps}} \simeq 17$, as in our experimental conditions. However, given the mass ratio between Ps^* and \bar{p} , the velocity of the heavy \bar{p} dominantly determines that of the resulting \bar{H} . While the production rate in our experimental apparatus would not be significantly influenced by cooling or not \bar{p} below few thousand K, we require \bar{p} cold enough (few hundred K, i.e., an almost negligible velocity compared to that of the orbital velocity of the e^+) for reasons related to our time-dependent \bar{H} detection sensitivity, as it will be clarified below (see section “Antihydrogen detection”).

Figure 1a, b shows the main elements of the AEGIS apparatus where the two “cold” species are prepared. All the charged particles, namely e^+ , \bar{p} and e^- (used to cool antiprotons by Coulomb collisions), are confined and manipulated inside Malmberg–Penning traps^{29,30} implemented through a series of cylindrical electrodes of optimized lengths, immersed in axial magnetic fields.

As detailed in “Methods” section, we catch and accumulate multiple bunches, typically 8, of antiprotons delivered by the AD facility in a trap region called \bar{p}_{trap} (15 mm radius, 470 mm length) and we cool them by collisions with e^- , which, in turn, lose their radial energy in the high (4.46 T) magnetic field. The mixed e^- and \bar{p} non-neutral plasma is then radially compressed^{34–36} and the \bar{p} ballistically transferred along the expanding magnetic field lines into the \bar{H}_{trap}^f region (5 mm radius, 25 mm length) located in a 1 T magnetic field, where further cooling with another e^- plasma takes place.

At the end of the preparation procedure, we obtain up to $\simeq 8 \times 10^5$ \bar{p} trapped with about 10^6 e^- in a quasi-harmonic potential well ready for \bar{H} formation.

We obtain the radial shape of the plasma with an imaging system made of a downstream on-axis micro-channel plate (MCP) (see “Methods” section) coupled to a phosphor screen read out by a CMOS camera, the number of e^- with Faraday cup signals and the number of \bar{p} with the ESDA. The size of the \bar{p} plasma is then estimated using a self-consistent thermal equilibrium model³⁷. Typically, the initial plasma radius is 1 mm and the semi-axial length is 2 mm. We keep \bar{p} confined for some thousand seconds during which we observe some radial transport with an increase of the radius by a factor 2 at maximum and some losses of \bar{p} 's.

The axial temperature $T_z = 440 \pm 80$ K of the \bar{p} plasma in the \bar{H}_{trap}^f is measured by slowly lowering the confining potential well, letting the \bar{p} escape the trap and fitting the time distribution of the first few \bar{p} leaving the trap as a function of the depth of axial

potential well³⁸ assuming that, as expected for a non-neutral trapped plasma in equilibrium, the axial energy follows a Maxwell distribution. The radial temperature T_r is expected to be similar to T_z , given that the collisionally induced energy re-equilibration rate in the plasma is higher than the (radial) cooling rate of the e^- .

During the \bar{p} preparation time, in the e^+ accumulation region (see Fig. 1a), e^+ emitted by a ^{22}Na radioactive source are slowed down by a solid Ne moderator and accumulated in a cylindrical Penning trap located in 0.1 T magnetic field. Once the \bar{p} are ready in the \bar{H}_{trap}^f , e^+ are extracted in bunches, accelerated in flight, and magnetically transported along an off-axis trajectory to the proximity of the trapped \bar{p} where they are implanted into the e^+ to Ps converter (see “Methods” section). Ps, formed with ~ 3 eV energy in the converter³⁹, slows down by collisions with the nanochannel walls until it is emitted into the vacuum. Ps is then excited by two laser pulses with 1.5 and 3 ns duration. The time when we fire the laser is the reference time for our pulsed scheme; this time is known with few ns accuracy.

Given the typical time spread of the e^+ pulse hitting the target of <10 ns, and the Ps cooling time in the target of the order of tens, the major uncertainty on the time when \bar{H} is formed is due to the spread in velocity, and thus in the time of flight, of the Ps^* reaching the \bar{p} cloud. With the Ps^* velocity distribution measured in our apparatus³², this spread in time results in a formation time distribution with a FWHM of ~ 80 ns (see details in “Methods” section).

Antihydrogen detection. Figure 1b shows the previously mentioned ESDA, which is made of 12 plastic scintillating (EJ200) slabs, each 1 cm thick and either 10 or 20 cm wide, coupled to two PMTs, one at each end, and shaped to cover a 120° arc of the cryostat containing the superconducting magnets. We use it to detect pions produced by the annihilations of \bar{p} and \bar{H} , as well as γ from e^+ and Ps annihilations. We modeled the response of the ESDA⁴⁰ and obtained its detection efficiency with a Monte Carlo simulation based on the Geant4⁴¹ software package: we generate \bar{p} (or e^+) annihilations in specific regions of the apparatus, track all the resulting particles including their interactions in all the materials and the full geometry of the apparatus, and finally count how many particles interact in the scintillators and record the corresponding energy deposit spectrum. As a reference, the \bar{H} detection efficiency, in the conditions detailed below, is 41.4%.

We continuously acquire—with a maximum rate of 10 MHz—the hit time of each pair of PMTs reading the same scintillator when the signals are in coincidence within 50 ns above an amplitude threshold of 50 mV, corresponding to an energy threshold of ~ 300 keV. These digital signals allow for continuous monitoring of the losses of trapped \bar{p} and also permit counting their number when they are deliberately dumped from the traps.

In the present experimental conditions, the expected number of \bar{H} is well below one atom for each \bar{H}_{cycle} ; this rare signal, consisting of the detection in the ESDA of pions stemming from \bar{H} annihilations, must be searched for above a large background induced in the ESDA by the intense, short pulse of e^+ hitting the target ~ 100 ns before the first Ps^* interact with \bar{p} . With $>90\%$ of the e^+ annihilating in the Ps conversion target, the total energy deposit of the resulting γ exceeds by some orders of magnitude that of the pions of a single \bar{H} . Furthermore, the corresponding e^+ annihilation signal in the ESDA shows long time tails due to after-pulses of the PMTs and delayed fluorescence of the scintillators that blind the detector for several hundred ns. As mentioned above, we can detect \bar{H} atoms only if they are slow

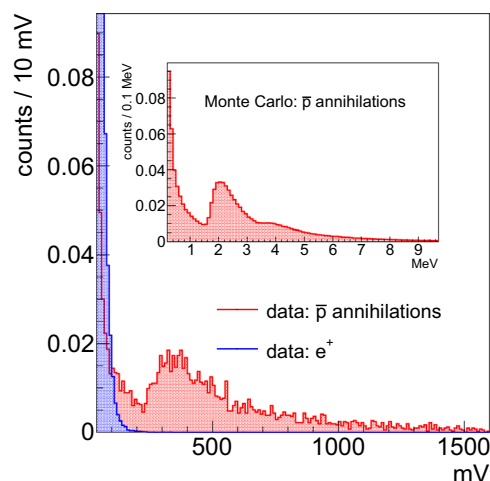


Fig. 2 External scintillator detector array (ESDA) amplitude spectra. The red plot in the main image shows the measured photomultiplier amplitude spectrum (mean value of the two photomultiplier signals contemporary within 50 ns) in the case of annihilation of \bar{p} on the walls of the \bar{H}_{trap}^f . This is the signal expected in case of \bar{H} production. The blue curve shows the distribution of the amplitudes of signals detected $1\ \mu\text{s}$ after the e^+ implantation in the target, without trapped \bar{p} . The two plots are normalized to unit area. The inset shows the distribution of the energy deposit in the ESDA obtained with a Geant4 simulation of \bar{p} annihilating on the wall of the \bar{H}_{trap}^f . The Monte Carlo and measured distributions are remarkably similar: the peak at 353 mV in the red plot of the main graph corresponds to the peak energy deposit of 2.14 MeV in the plot in the inset.

enough that their annihilation signal on the trap walls is generated after this blind time.

With the above-mentioned \bar{p} temperature and the geometry of our trap, we expect that the \bar{H} signal will appear within few μs from the laser firing time.

The scintillator pulse time distribution relative to the laser firing time does not provide a clean enough signature to uniquely identify \bar{H} annihilations; however, the complementary information of the scintillator signal amplitude is sufficient to eliminate the potential e^+ injection-linked background, which does not contain signals due to minimum ionizing charged particles. Specifically, the output of the PMTs is sampled and digitized—with 250 MHz frequency—in a time window of $650\ \mu\text{s}$ around the laser firing time (from $100\ \mu\text{s}$ before to $550\ \mu\text{s}$ after). The amplitude of simultaneous—within 50 ns—PMT signals read from the same scintillator is then used to differentiate pions originating from \bar{H} annihilations from late γ signals or delayed fluorescence of the scintillator induced by e^+ . As Fig. 2 shows and as expected for minimum ionizing particles, signals induced by pions originating from \bar{p} annihilations are characterized by a larger energy deposit in the scintillator—and thus larger amplitudes—than signals following the e^+ impact on the e^+ to Ps converter. An appropriate cut on both the signal amplitude and the delay after the laser firing time is a powerful tool to eliminate the background induced by e^+ . Note that requiring time-coincident signals in both PMT’s of a given scintillator allows to efficiently reject backgrounds stemming from random signals, such as after-pulses in either PMT.

The antihydrogen signal. We have alternated \bar{H} production cycles with the Ps excitation laser in the nominal conditions ($1\bar{p}e^+$

data set) with cycles without shining the laser ($\bar{p}e^+$ data set). Data with laser on and trapped \bar{p} but without extracting e^+ from the accumulator ($l\bar{p}$ data set) have also been acquired. Candidate \bar{H} signals are time-coincident pulses detected in any scintillator with mean amplitude—see Fig. 2—above a given threshold V_{\min} , measured within a time window ΔT^S starting after a time T_{\min} from the laser firing time, defined here as $t = 0$. The choice of T_{\min} and V_{\min} is a tradeoff between increasing the \bar{H} detection efficiency and reducing the background due to the e^+ -induced signals. With $T_{\min} = 1 \mu\text{s}$, $V_{\min} = 250 \text{ mV}$, and ΔT^S of some μs , the number of candidates that we find in a data set including only e^+ (without \bar{p}) is statistically consistent with that measured with cosmic rays $(1.94 \pm 0.03) \times 10^{-4} \text{ counts } \mu\text{s}^{-1}$, thus showing that the background induced by the e^+ signal with these data selection criteria is negligible. With the above-defined values of V_{\min} and T_{\min} , both the rate and the amplitude distributions of cosmic ray signals detected after the e^+ pulse are fully compatible with those measured in the absence of injected e^+ . We thus conclude that the adopted analysis criteria ensure that the ESDA response is not influenced by the e^+ burst.

We call the time window ΔT^S signal region (S) and the regions with the time between -101 and $-1 \mu\text{s}$ and 50 and $550 \mu\text{s}$ control regions (C). The control region has a total length of $600 \mu\text{s}$, while the signal region can be varied between ~ 5 and $\sim 25 \mu\text{s}$.

Figure 3a–c shows the time distribution of the coincident pulses with $V_{\min} = 250 \text{ mV}$ and $T_{\min} = 1 \mu\text{s}$ in the entire time window of $650 \mu\text{s}$ for the three data sets ($l\bar{p}e^+$, $\bar{p}e^+$, $l\bar{p}$) of measurements; given that the afterglow contribution from the e^+ is negligible, the number of counts includes only contributions from cosmic rays, \bar{p} annihilations as well as any \bar{H} annihilations.

The \bar{H} signal should show up as an excess in the number of events in the signal region with respect to the mean value of the events in the control region only in the data set $l\bar{p}e^+$. The comparison between the plots referring to the $l\bar{p}e^+$ and $\bar{p}e^+$ samples in Fig. 3a, b clearly suggests the presence of this expected excess in a signal region few tens μs long. Figure 3c also shows (for a larger number of trials than for the $l\bar{p}e^+$ data set) some excess counts in the signal region with respect to the mean value of counts in the control region in the $l\bar{p}$ data set. Contrary to the cosmic background and continuous annihilations, which have a constant rate, these time-dependent counts represent the only relevant background in our measurement. We interpreted them as annihilations of \bar{p} following the desorption of gas from the cryogenic walls hit by the laser (see “Methods” section).

In order to quantify the evidence of \bar{H} formation, we have assumed as a null hypothesis the absence of \bar{H} signal in the sample $l\bar{p}e^+$ and determined the number of counts expected in the S region of this sample. Finally, this number has been compared with the measured one. Referring to the two samples $l\bar{p}$ and $l\bar{p}e^+$ we consider the measured number of counts ($n_{l\bar{p}}^S$, $n_{l\bar{p}e^+}^S$) in the signal and in the control ($n_{l\bar{p}}^C$, $n_{l\bar{p}e^+}^C$) region (see Table 1). In both the regions S and C, the measured values take a contribution from the counts n_{μ} due to cosmic rays (muons) and from the number of \bar{p} annihilation in the trap not related to the presence of the laser, n_{trap} . We assume that n_{trap} and n_{μ} scale as the duration of the specific C and S regions. The C region is free from the contribution, called here n_{gas} , due to annihilations of \bar{p} on the laser desorbed gas as evidenced by the statistical consistency of the counts in the C region obtained with the samples without and with laser—last two lines of column 6 in Table 1—once the cosmic ray contribution is subtracted and then they are rescaled to the same number of \bar{p} .

In the S region, in both the samples $l\bar{p}$ and $l\bar{p}e^+$, we have, in addition to the previous contributions, the n_{gas} background and,

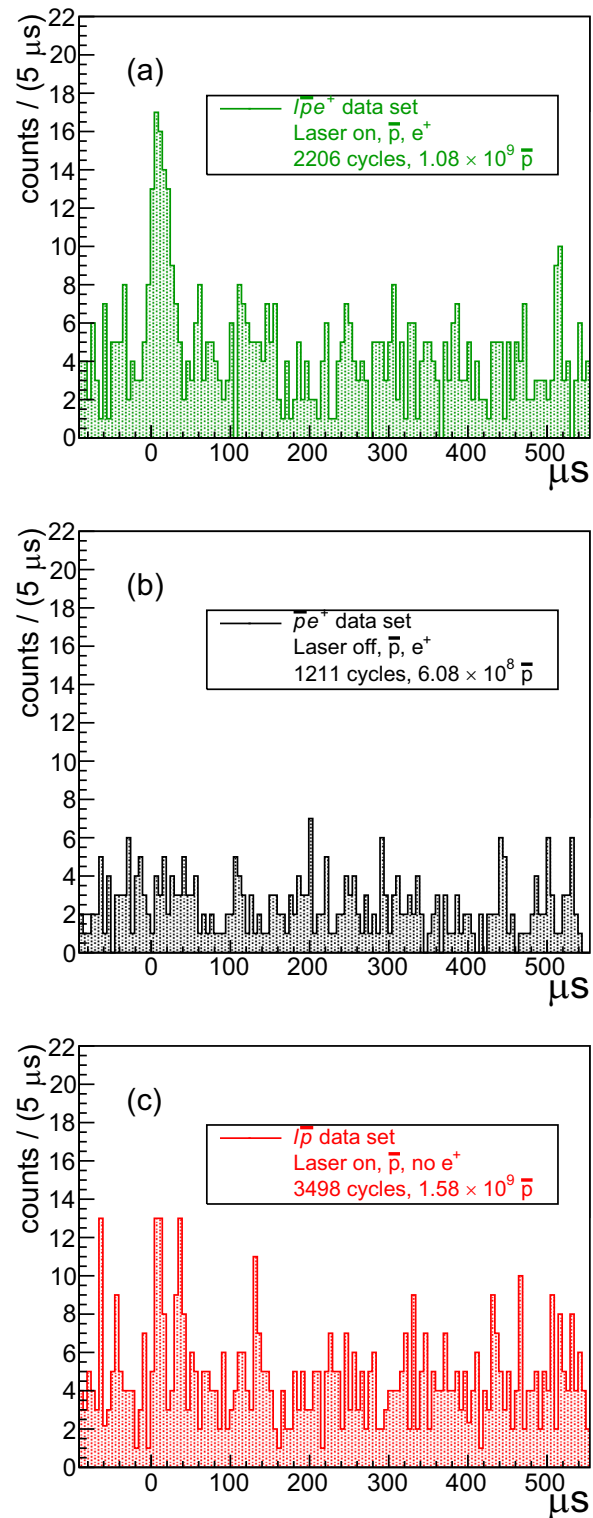


Fig. 3 Time distribution of external detector scintillator array (ESDA) pulses. We show the distributions of the coincident pulses with mean amplitude $>250 \text{ mV}$, detected after $1 \mu\text{s}$ from the laser firing time for the three samples of data: **a** $l\bar{p}e^+$, **b** $\bar{p}e^+$, and **c** $l\bar{p}$. Note that the number of \bar{p} and \bar{H}_{cycle} are different in the three samples and that the number of counts due to cosmic rays scales linearly with the number of \bar{H}_{cycle} , while the counts due to annihilations are proportional to the total \bar{p} number. The effect of the resulting normalization is mainly to reduce the counts in **c** relative to those of **a** by a factor of ~ 1.5 , and to increase the counts in **b** relative to those of **a** by a factor of ~ 1.7 .

Table 1 Summary of the measured counts.

Sample X	\bar{H}_{cycle}	\bar{p} number N_X	Counts in the S interval n^S	Cosmic ray counts in the S interval n_{μ}^S	Counts in the C interval n^C	Excess counts (S interval), normalized to $N_{\bar{p}e^+}$ $\left(n^S - n^C \frac{\Delta T^S}{\Delta T^C}\right) \frac{N_{\bar{p}e^+}}{N_X}$	\bar{H} number
\bar{p}	3498	$(1.58 \pm 0.01) \times 10^9$	42.0 ± 6.5	17.0 ± 0.3	528 ± 23	13.7 ± 4.5	
$\bar{p}e^+$	1211	$(6.08 \pm 0.07) \times 10^8$	16.0 ± 4.0	5.8 ± 0.1	278 ± 17	1.7 ± 1.6	
$\bar{p}e^+$	2206	$(1.08 \pm 0.01) \times 10^9$	79.0 ± 8.9	10.7 ± 0.2	475 ± 22	59.2 ± 8.9	45.6 ± 10.0

The table reports, for each sample, the number of experimental cycles \bar{H}_{cycle} , the number of antiprotons N_X , where X stands for \bar{p} , $\bar{p}e^+$, $\bar{p}e^+$, the number of counts n^S measured in the corresponding 25- μs -long S region, and the mean number n_{μ}^S of counts due to cosmic rays in the S region calculated from an independent measurement of the cosmic rate with the adopted analysis cuts. As discussed in the main text, the value of n_{μ}^S is not directly used in the extraction of the \bar{H} signal; it is reported here for clarity. Column 6 shows the number of counts in the C region. Column 7 reports the excess of counts in the S region, obtained as the difference between n^S and the number of counts n^C rescaled to the S region time length, normalized to the number of antiprotons measured in the sample $\bar{p}e^+$. This excess of counts is consistent with zero only for the sample $\bar{p}e^+$, while it is positive for both the sample \bar{p} (because of \bar{p} losses due to the laser-induced outgassing) and $\bar{p}e^+$, where in addition, we have \bar{H} production. The detected number of \bar{H} is obtained as the difference between the normalized excess of counts in the $\bar{p}e^+$ and \bar{p} samples.

in the $\bar{p}e^+$, the counts due to \bar{H} annihilation, $n_{\bar{H}}$. As discussed in the “Methods” section, n_{gas} is proportional to the numbers $N_{\bar{p}}$, $N_{\bar{p}e^+}$ of trapped \bar{p} through a factor ϵ . This factor can be determined using the data of the \bar{p} sample ($n_{\text{gas}} = \epsilon N_{\bar{p}}$) and used to predict (see “Methods” for details) the number of counts n_{exp}^S we would expect in the S region of the sample $\bar{p}e^+$ in absence of \bar{H} production ($n_{\bar{H}} = 0$):

$$n_{\text{exp}}^S = \left[n_{\bar{p}e^+}^C \frac{\Delta T^S}{\Delta T^C} + \left(n_{\bar{p}}^S - n_{\bar{p}}^C \frac{\Delta T^S}{\Delta T^C} \right) \frac{N_{\bar{p}e^+}}{N_{\bar{p}}} \right], \quad (2)$$

where $N_{\bar{p}e^+}$ and $N_{\bar{p}}$ represent the sum over all of the number of \bar{p} in the two data samples.

If the null hypothesis ($n_{\bar{H}} = 0$) is true then n_{exp}^S would be statistically compatible with the measured value $n_{\bar{p}e^+}^S$. The measured number of counts in an S region 25 μs long—extending from 1 to 26 μs after the laser pulse—is $n_{\bar{p}e^+}^S = 79.0 \pm 8.9$, while $n_{\text{exp}}^S = 33.4 \pm 4.6$. Consequently, we obtain a p value of 6.6×10^{-7} , and the hypothesis of the absence of signal is rejected with 4.8σ (local significance). The number of counts above background, and the significance of the signal above 4σ , is robust against variations in the choice of the width or offset of the S interval.

The number of detected antihydrogen atoms in the 25- μs -wide S region is 45.6 ± 10.0 ; taking into account the detection efficiency, this corresponds to 110 ± 25 produced atoms. This number agrees with the prediction of a dedicated Monte Carlo (see “Methods” section) in which we model the Ps excitation process, we include all geometrical details of the interaction region, the number and shape of the antiproton plasmas, the number of P, and its measured velocity as well as the cross-section from ref. 26, thus indicating that the role of the relevant parameters is under control.

The temporal evolution of the signal in Fig. 3a is unexpectedly long if the only relevant parameter were the above-mentioned value of the \bar{p} temperature. Indeed, for a \bar{p} temperature of ~ 400 K, formation with a burst of Ps* with our measured range of velocities should result in a few μs wide signal, while the experimental one extends up to 25 μs . Due to our small sample size, it was not possible to investigate this effect more deeply. While both a lower \bar{p} temperature or the presence of a small fraction of Ps* with very low ($< 10^4$ m s $^{-1}$) velocity would result in an enhanced signal at later than expected times, one appealing explanation is related to the possibility that the Rydberg \bar{H} atoms could be reflected from the electrode metallic surfaces. The

interaction of a Rydberg \bar{H} with a metallic surface is first due to the electrostatic interaction with its induced image charge. The large dipole of a Rydberg state induces a charge polarization in a metallic bulk that results in an attractive net force⁴². At the smaller end of the range of separations, the influence of the image charge interactions becomes stronger, and the positron could potentially be able to pass over or tunnel through the potential barrier into the conduction band producing annihilation. However, because certain metals have negative work functions for e^+ , the positron can also be reflected from the corresponding surfaces and so the whole Rydberg atom with it. Note that the trap electrodes are gold plated and negative values of the e^+ work function in case of gold are reported in the literature⁴³. This would be the antimatter counterpart of the reflection of Rydberg (matter) atoms from negative electron affinity surfaces described in ref. 44. Obviously, this putative effect requires more study to be confirmed, which also requires taking into account the presence of the electric and magnetic fields, but we highlight the fact that Rydberg \bar{H} atoms can be expected to behave differently from Rydberg H near a surface.

The presence of the \bar{H} signal is further supported by a second, independent detector (fast cryogenic tracker—FACT^{45,46}) capable of track reconstruction, and operated simultaneously with the ESDA. It consists of two concentric double-layer cylinders of scintillating fibers readout through arrays of silicon photomultipliers, surrounding the \bar{H}_{trap}^f and Ps production target (see Fig. 1a). This detector is affected by the initial e^+ annihilation pulse more severely than the ESDA due to its proximity to the Ps production region: for the first 10 μs after the injection pulse, it exhibits a too high count rate for stand-alone use. However, owing to its high—5 ns—temporal resolution, requiring a coincidence within 10 ns with a signal in the ESDA allowed identifying a number of potential track candidates and determining the z -coordinate of their intersection with the axis of the apparatus. Figure 4 shows the resulting distribution of the weighted track z -coordinates, where the central peak coincides with the position of the antiproton cloud, proof that the hits recorded in the ESDA stem from annihilation events.

While the spatial resolution of the tracking detector is insufficient to differentiate antihydrogen annihilations on the electrodes from antiproton annihilations at the position of the \bar{p} cloud, the temporal constraint of the pulsed scheme provides a clean time window in which \bar{H} annihilations could thus be identified. Together with the independent detection relying on discrimination of the signal amplitude between pion-induced

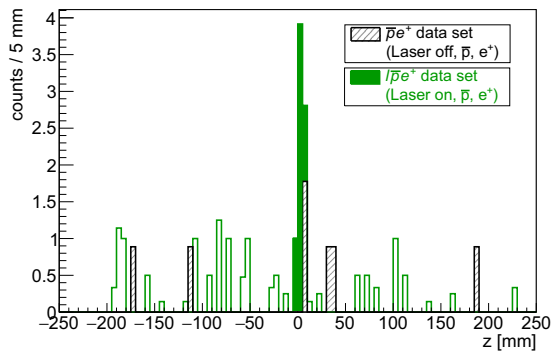


Fig. 4 Distribution of the z -coordinates of tracks reconstructed with the fast cryogenic detector (FACT). The plot shows the distribution of the z -coordinates of charged particle tracks reconstructed from hits detected in the two layers of the FACT detector in temporal coincidence ($\Delta t = \pm 5$ ns) with hits of the external detector scintillator array (ESDA). For this combined analysis, we used a mean ESDA amplitude of 150 mV, lower than that used in the ESDA-only analysis. The antiproton plasma is centered at $z = 0$. The distributions for the two samples are rescaled to the same number of antiprotons; furthermore, each track is weighted to account for combinatorial ambiguities (several hits may fire in the same temporal coincidence window, particularly at early times).

signals and any background subsequent to the intense e^+ pulse, clear evidence for the detection of a pulsed \bar{p} annihilation signal stemming from the region in which the \bar{H} annihilation signal is expected, which is furthermore compatible with the observed ESDA rates and our understanding of the processes involved in \bar{H} formation, has been obtained. The available statistics are, however, insufficient to extract a possible broadening of the z -distribution with time (as would be expected in the case of reflected Rydberg \bar{H} atoms).

Discussion

The present AEGIS result builds on earlier advances and extends them to experimentally demonstrate the formation of \bar{H} with the most precise time tagging ever reached, to the best of our knowledge. Owing to the pulsed production method made possible by a charge exchange reaction with laser-excited Ps, several promising experimental venues are opened.

The first one regards the temperature of the \bar{H} : gravity measurements require ultracold \bar{H} with temperatures in the sub-kelvin range. The charge exchange method, wherein \bar{H} is produced with the temperature of the stationary \bar{p} (with the recoil energy from the interaction with Ps accounting only for few tens $m s^{-1}$ for the range of the Ps parameters discussed in this paper), offers a more direct route towards ultracold \bar{H} than 3-body recombination. Consequently, obtaining cold \bar{H} relies on the ability to cool only one species, the \bar{p} . On the contrary, producing cold \bar{H} via 3-body recombination requires cooling both \bar{p} and e^+ . Efforts to develop methods able to cool \bar{p} to sub-kelvin temperatures are underway and are compatible with production of \bar{H} through charge exchange^{47–49} but not with the 3-body recombination scheme. These routes are complementary to the current efforts and achievements on reaching low \bar{H} temperature in the 3-body scheme. Currently, daily accumulation of ~ 1000 \bar{H} with 0.5 K in a trap has been demonstrated, and furthermore, first laser cooling of trapped \bar{H} has been reported⁵⁰. Laser cooling of untrapped atoms is currently not achievable as it would require

suitable, currently not yet developed, pulsed Lyman- α laser sources⁵¹.

Second, although 3-body recombination and charge exchange both produce \bar{H} in Rydberg states, in the charge exchange reaction the peak value and width of the distribution of the \bar{H} principal quantum number can be tuned by controlling the principal quantum number and velocity of the Ps^* . The peak value is $\sim \sqrt{2}n_{Ps}$ and the distribution is particularly narrow in collisions of \bar{p} with low-velocity Ps^* ²⁶ (below $\approx 10^4 m s^{-1}$ for $n_{Ps} \approx 17$). The distribution of Rydberg states resulting from the 3-body process is broad, peaked to high values of the principal quantum numbers and it cannot be easily tuned^{52,53}.

Thirdly, the pulsed scheme permits for targeted manipulation of the formed antihydrogen atoms which, with experimentally interesting values of the \bar{H} quantum numbers and velocities, are not collisionally de-excited within the mixed $\bar{p} - e^-$ plasma²². Through the use of laser pulses, properly synchronized with the production time, \bar{H}^* could be de-excited⁵⁴ from long-lifetime Rydberg states towards the fundamental state. \bar{H} in the fundamental state is desirable to reduce systematic effects due to gradients of magnetic fields in gravity experiments or to perform high-precision hyperfine splitting measurements⁵⁵. Alternatively, again owing to the knowledge of the production time, switching the \bar{p} trapping voltages to a configuration able to accelerate Rydberg \bar{H} ⁵⁶ in one direction opens the possibility to form a horizontally traveling atomic beam.

Finally, the pulsed scheme opens the possibility of re-exciting \bar{H} from the fundamental state reached after the de-excitation pulses to a defined state, thus opening the possibility for an efficient transport of \bar{H} with electric or magnetic field gradients⁵⁷.

Although the current production rate is low, a number of straightforward improvements allows boosting it substantially. There is room to significantly increase the number of e^+ , and then of Ps^* , available at each cycle, and independently, the number of \bar{p} . In fact, with the availability of very low-energy antiprotons made possible by the ELENA upgrade⁵⁸ to the AD, the antiproton trapping efficiency should increase by two orders of magnitude. A further important optimization is provided by a modified trap and Ps conversion target geometry with reduced solid angle losses of Ps, and with the e^+ to Ps converter mounted on the trap axis which should allow working with more highly excited Ps Rydberg states. The current limit of $n_{Ps} = 17$ is due to the dynamical field ionization in the effective electric field resulting from the motion of Ps^* orthogonal to the magnetic field. In addition, by implanting the positrons more deeply in the conversion target, thereby improving the Ps thermalization process, the low-velocity fraction of Ps can be increased. Both factors—higher Rydberg states and lower Ps^* velocity—contribute to increase in the number of \bar{H} that can be produced with a given \bar{p} plasma, owing to the scaling law of the cross-section^{26,27}.

The demonstration of the production of pulsed \bar{H} as reported in this paper is a major milestone in the AEGIS experimental program. The described increase of the \bar{H} production rate coupled with efficient methods of \bar{H} beam formation—under development—paves the way towards a direct g measurement.

Methods

Detectors. In addition to the scintillator-based ESDA and FACT detectors, further devices are used to image or detect charged particles during various stages of the manipulations. Particles trapped in different regions of the apparatus can be imaged on an MCP coupled to a phosphor screen, both at 10K, mounted downstream of the \bar{H}_{trap}^f and read out by a CMOS camera at room temperature. Lowering the potential wells in which they are held allows them to reach the MCP by following the magnetic field lines.

Several calibration data are collected, typically with electrons, with different bias voltages on the MCP to establish the working point where the MCP responds linearly to the incoming flux of particles. The particle radial distribution, integrated along the z -direction, is recorded in this manner. The imaging system is also used to detect e^+ resulting from ionization of Ps^* ⁵⁹.

Several scintillators placed around the e^+ accumulation and transfer setup are devoted to the optimization of these devices.

Faraday cups, connected to calibrated charge sensitive amplifiers, provide the number of e^- and e^+ with a sensitivity limit of 5×10^5 particles. Positrons passing through the transfer line are also detected and counted by reading with a low noise amplifier, in a non-destructive manner, the image charges in the accelerating tube.

Finally, the charge measured by the PMTs of ESDA, together with the Geant4 simulation, furnishes an additional independent measure of the e^+ reaching the Ps formation target in agreement with the independent Faraday cup and image charge signals.

\bar{p} Manipulation. Pulses of antiprotons (5.3 MeV kinetic energy, $\approx 3 \times 10^7$ \bar{p} per pulse, <500 ns length²³) are delivered every ≈ 100 s to the AEGIS apparatus by the AD facility of CERN. After having been slowed down by their passage through a set of Al and Si foils, $\approx 4 \times 10^5$ \bar{p} per shot with energies up to 10 keV are trapped in flight in the \bar{p}_{trap} —in which a plasma of $\approx 2 \times 10^8$ e^- is preloaded into an inner potential well of 3 cm length—by first setting to 10 kV the end electrode of the \bar{p}_{trap} and then by rapidly (10–20 ns) switching the entrance electrode to the same voltage value, as pioneered in ref. 60.

The trapped antiprotons dissipate their energy by collisions with the electrons, which in turn, due to their low mass, efficiently cool by emitting cyclotron radiation in the high magnetic field. After ~ 20 s, $\approx 70\%$ of the trapped \bar{p} are cooled to sub-eV energies and are confined together with the electrons in the inner potential well. The catching and cooling procedure is typically repeated eight times, always adding the newly trapped and cooled \bar{p} on top of those already stored in the \bar{p}_{trap} ⁶¹.

The mixed cold \bar{p} and e^- plasma is radially compressed by using radio-frequency voltages applied to a trap electrode that is radially split into four sectors³⁴, allowing to reach a plasma radius <0.2 mm, more than 10 times smaller than the starting value.

Finally, using synchronized voltage pulses, \bar{p} are launched from the \bar{p}_{trap} and re-trapped in flight in the \bar{H}_{trap}^f after a travel of ~ 1.5 m along the expanding magnetic field lines.

This ballistic transfer procedure re-heats the \bar{p} to tens of eV and it does not allow to simultaneously transfer the lighter e^- . Electrons ($\approx 2 \times 10^7$) are thus independently added on top of the \bar{p} in the \bar{H}_{trap}^f and the two plasmas cool again for ~ 10 s. We progressively reduce the number of e^- to decrease the plasma density and to avoid the centrifugal separation of the two species³⁰, allowing at every step the system to thermalize. With eight AD shots, we end up with $\approx 8 \times 10^5$ \bar{p} (with $\approx 10^6$ e^-) in the \bar{H}_{trap}^f corresponding to an overall efficiency of the procedure of stacking, transfer, and re-cooling in 1 T magnetic field $>35\%$.

Ps formation and excitation to Rydberg levels. The experimental methodology used to produce clouds of Rydberg Ps atoms consists of several steps detailed in previous works^{33,62}. Referring to Fig. 1a, in the e^+ accumulation region of AEGIS, e^+ , emitted from a 25 mCi ^{22}Na source, are moderated by solid neon, trapped, and finally accumulated in the e_{trap}^+ ⁶² using cooling by buffer gas collisions⁶³. Positrons are extracted from the e_{trap}^+ in bunches of variable intensity (we used $\sim 2 \times 10^6$ e^+ per bunch in the \bar{H} production experiments) characterized by an ~ 300 eV mean axial energy. They are guided into the main magnetic field of the experiment by a pulsed magnetic transfer line, allowing vertical and horizontal tuning of their injection position. Along this transfer section, a 70-cm-long electrode is pulsed to 4.3 kV synchronously to the e^+ passage (i.e., when the complete e^+ bunch is contained within the electrode) to increase their axial flight energy to a level suitable for efficient Ps formation by implantation in the nanochanneled e^+ to Ps converter installed above the \bar{H}_{trap}^f . Positrons reach the converter by following an off-axis trajectory through the 4.46 and 1 T magnetic fields practically conserving the time spread present when they are inside the accelerating electrode (<10 ns FWHM).

The number of e^+ reaching the target during each \bar{H}_{cycle} is measured through the charge collected by one of the PMT of the ESDA scintillators normalized with the Geant4 Monte Carlo prediction. The results are in agreement with independent control measurements obtained by dumping the e^+ on axis and detecting the collected charge with a Faraday cup close to the target region. On average, 2×10^6 e^+ (the number distribution has an FWHM of 44%) are available for all cycles.

The converter is constituted by a Si(111) p-type crystal with nanochannels produced via electrochemical etching and subsequently oxidized in air²⁸. Ps exiting the converter is subsequently laser excited to $n_{\text{Ps}} = 3$ by means of a broadband UV laser pulse with 205.045 nm wavelength, 1.5 ns duration, and ~ 40 μJ energy and to Rydberg levels with n_{Ps} ranging in the interval 14–22 (typically 17) by means of a second synchronized broadband IR laser pulse (3 ns long, tunable from 1680 to 1720 nm, 1.6 mJ energy).

In alternative to the off-axis trajectory, e^+ was optionally transferred along an on-axis trajectory toward a Faraday cup or the MCP imaging system for precise alignment and diagnostics purposes.

During a series of test experiments, not devoted to \bar{H} production, we have established the yield of Ps emission of $(7.0 \pm 2.5)\%$ ³¹ by analyzing the time distribution of γ following the e^+ implantation as detected by one of the scintillators of the ESDA⁶⁴.

Also, we have combined the UV laser (with the IR laser off) with a second synchronous intense laser pulse at 1064 nm to selectively photo-ionize all Ps atoms excited to $n_{\text{Ps}} = 3$ and to measure the excitation efficiency, found to be $(8.1 \pm 3.0)\%$ ³¹.

The bandwidth of the UV laser (120 GHz) is smaller than the Doppler width (~ 500 GHz) of the 1S–3P transition induced by the velocity spread of Ps; consequently, we do not excite all Ps atoms along the laser path shown in Fig. 1b: instead, by appropriately tuning the UV wavelength we could optimize the excitation efficiency targeting specifically the Ps heading towards the entrance grid of the \bar{H}_{trap}^f .

The on-axis MCP detector offered a very sensitive and high-resolution imaging diagnostics (with ~ 100 μm resolution⁵⁹) of the photodissociated e^+ , allowing the UV wavelength to be accurately set with the direct feedback of the excited Ps fraction alignment before \bar{H} production trials. This detector also allowed a direct characterization³² of the velocity distribution of Ps atoms emerging from the e^+ to Ps converter.

A fraction of the Rydberg Ps atoms immediately ionizes due to the presence of the 1 T magnetic field. Indeed, Ps^* atoms experience an induced electric field $\vec{E} = -\vec{v}_{\text{Ps}} \times \vec{B}$ due to their motion in a magnetic field, which causes field ionization of sufficiently high n_{Ps} Rydberg atoms^{65,66}. n_{Ps} was thus set to 17 during \bar{H} production trials, a compromise between field-ionization losses ($\sim 30\%$ of the total available atoms³²) and the n_{Ps}^4 gain in the \bar{H} formation cross-section²⁶. Note that any field ionization of Ps^* , at this addressed range around $n_{\text{Ps}} = 17$, has a negligible impact on the \bar{H} formation because it affects only those Ps^* with strongly suppressed cross-section.

Monte Carlo prediction of the \bar{H} signal. We have developed a dedicated Monte Carlo⁶⁷ simulation modeling the main physical processes playing a role in the experiment and including the full 3D geometry of the e^+ to Ps converter and of the antiproton trap region.

In these simulations, a Ps cloud was generated at the estimated positron target entrance position, with appropriate Ps spatial and temporal spread (we do not model the Ps formation and cooling in the target).

Each single Ps is given a velocity randomly extracted from the experimental distribution reported in ref. 32 and is propagated along a straight line with its standard lifetime in a vacuum (142 ns) unless it reaches some material surface.

The subsequent interaction with the laser pulses is simulated taking into account the UV laser parameters (that play a greater role than those of the IR laser), that is, laser relative timing with respect to the average Ps emission time, with the measured (two-dimensional Gaussian) spatial intensity and temporal profile. Since the pulse length is relatively short compared to the typical motion of each Ps in that time, the Ps cloud is practically frozen at the moment of the laser pulse, and some of the Ps atoms are subsequently excited to the Rydberg level $n_{\text{Ps}} = 17$. The interaction of each Ps atom with the laser is implemented by a model based on incoherent excitation, that is, the probability to produce a Rydberg Ps depends mainly on the Doppler effect and on the local fluence of the laser pulse seen by the Ps atom itself.

Each Ps^* atom is then propagated along the original trajectory with unchanged velocity (recoil effects are neglected, as well as the influence of the magnetic and electric fields) until it reaches a material surface or interacts with the \bar{p} plasma.

Typically, with our experimental parameters, in a relatively large range of tuneable experimental settings, simulations indicate that $\sim 10\%$ of the Ps atoms reach Rydberg states (in agreement with what is measured). As already discussed, the fraction of excited Ps is not uniformly distributed within the Ps cloud as the lasers address only the Ps traveling toward the trap. About 10% of excited Ps may pass through the \bar{p} plasma (simulated with the mean values of the expected position, number, size, density, and temperature). Calculating the charge exchange probability through the charge exchange cross-section of ref. 26, we find that the average interaction probability is $\sim 5 \times 10^{-5}$ per single Ps^* atom traversing the \bar{p} cloud. This number includes the losses of Ps due to self-ionization in the magnetic field. In summary, the Monte Carlo result implies that with 2×10^6 e^+ per cycle on average (providing 1.4×10^5 Ps per cycle), the number of Ps^* traversing the \bar{p} cloud is $\sim 1.4 \times 10^3$ and the number of expected \bar{H} is $\sim 0.07/\bar{H}_{\text{cycle}}$. Then, with 2206 \bar{H}_{cycle} , the expected total number of produced \bar{H} is ≈ 100 , in agreement with the observation.

The distribution of the time of \bar{H} formation is built evaluating the time of flight of those Ps^* that form \bar{H} . The predicted time distribution typically peaks 125–150 ns after the laser firing time and it has a FWHM of ~ 80 ns. The increase of the cross-section at low velocity makes the distribution asymmetric, resulting in a tail toward high time values. As reported in the main text, 90% of the \bar{H} is produced within an ~ 250 -ns-wide time window. The \bar{H} production time is not directly experimentally observable: we can only measure the time when \bar{H} annihilates. However, the distribution of the time of \bar{H} formation is a robust prediction of the

Monte Carlo: it only depends on the experimentally determined Ps^* velocity, geometrical parameters, and on the variation of the cross-section with the Ps^* velocity.

\bar{H} signal and error budget. Referring to the sample $l\bar{p}$, in the signal (S) and in the control (C) region, we can write the measured number of counts $n_{l\bar{p}}^S$ and $n_{l\bar{p}}^C$ as

$$n_{l\bar{p}}^S = (n_{\mu} + n_{\text{trap}} + n_{\text{gas}})_{l\bar{p}}^S, \quad (3)$$

$$n_{l\bar{p}}^C = (n_{\mu} + n_{\text{trap}})_{l\bar{p}}^C, \quad (4)$$

where n_{μ} and n_{trap} are the number of counts due to cosmic rays (muons) and to \bar{p} annihilation in the trap not related to the presence of the laser, while finally, n_{gas} is the number of counts due to \bar{p} annihilation on the laser-induced desorbed gas. As discussed in the subsection “Laser-induced \bar{p} losses”, n_{gas} is proportional to the number $N_{l\bar{p}}$ of trapped \bar{p} , $n_{\text{gas}} = \epsilon N_{l\bar{p}}$. The factor ϵ can be determined using the relations in Eqs. (3) and (4) taking also into account that n_{μ} and n_{trap} are proportional to the duration of the time interval during which they are evaluated:

$$\epsilon = \frac{1}{N_{l\bar{p}}} \left(n_{l\bar{p}}^S - n_{l\bar{p}}^C \frac{\Delta T^S}{\Delta T^C} \right). \quad (5)$$

A couple of relations similar to Eq. (3) and (4) can be written for the sample $l\bar{p}e^+$ including the presence of the \bar{H} signal. We call $n_{\bar{H}}$ the number of counts due to \bar{H} and $N_{l\bar{p}e^+}$ the total number of \bar{p} in the data set $l\bar{p}e^+$:

$$n_{l\bar{p}e^+}^S = (n_{\mu} + n_{\text{trap}} + n_{\text{gas}})_{l\bar{p}e^+}^S + n_{\bar{H}}, \quad (6)$$

$$n_{l\bar{p}e^+}^C = (n_{\mu} + n_{\text{trap}})_{l\bar{p}e^+}^C. \quad (7)$$

Recalling that n_{gas} is proportional to $N_{l\bar{p}e^+}$, and using the expression of ϵ obtained in Eq. (5), we can thus estimate the number of counts n_{exp}^S we would expect in the S region in the absence of \bar{H} production in the sample $l\bar{p}e^+$ to be:

$$n_{\text{exp}}^S = \left[n_{l\bar{p}e^+}^C \frac{\Delta T^S}{\Delta T^C} + \left(n_{l\bar{p}}^S - n_{l\bar{p}}^C \frac{\Delta T^S}{\Delta T^C} \right) \frac{N_{l\bar{p}e^+}}{N_{l\bar{p}}} \right]. \quad (8)$$

The total number of interacting antiprotons in the $l\bar{p}$ sample, as calculated using the procedure explained below, is higher than in the $l\bar{p}e^+$ data set ($N_{l\bar{p}e^+} = 1.08 \times 10^9$, $N_{l\bar{p}} = 1.58 \times 10^9$). Table 1 summarizes the relevant number of counts in the S and C regions of the three data samples.

Our measurement relies on the comparison of $n_{l\bar{p}e^+}^S$ with n_{exp}^S . The standard deviation on $n_{l\bar{p}e^+}^S$ is simply its square root since we have assumed a Poissonian distribution. To estimate the uncertainty on n_{exp}^S we propagated the errors in Eqn. (2). The standard deviations on $n_{l\bar{p}e^+}^C$, $n_{l\bar{p}}^C$ and $n_{l\bar{p}}^S$ are again the square roots of themselves. It is important here to note that the error on $n_{l\bar{p}}^S$, with $n_{l\bar{p}}^S = 42$, is the dominant one; all the other contributions are negligible.

As anticipated, $N_{l\bar{p}e^+}$ and $N_{l\bar{p}}$ represent the sum over all the \bar{H}_{cycle} of the number of \bar{p} in the two data samples. We directly measure the number of surviving \bar{p} after several \bar{H} production cycles by emptying the trap and counting the annihilation pions using the ESDA. The estimate of the initial number of \bar{p} available in the trap is based on the proportionality—which we have verified in a series of dedicated measurements—between the losses of \bar{p} detected during the transfer from the \bar{p}_{trap} to the \bar{H}_{trap}^f and the number of \bar{p} left in the \bar{H}_{trap}^f and available for the first \bar{H} production cycle. Knowing the initial and final number of \bar{p} and assuming an exponential loss with time, we obtain the number of available \bar{p} at every cycle. Assuming instead losses that would be linear with time results in a systematic error of 3.5% on the measurement of both $N_{l\bar{p}e^+}$ and $N_{l\bar{p}}$. Statistical uncertainties are negligible.

The total uncertainty on n_{exp}^S has been estimated by using a Monte Carlo method, to take into account the correlation between the systematic uncertainties on $N_{l\bar{p}e^+}$ and $N_{l\bar{p}}$.

Laser-induced \bar{p} losses. The environment surrounding the \bar{H}_{trap}^f is pumped down during the preparatory phase of the experiment, and it is then cooled to a temperature of 10 K and kept cold for many months. All the cold surfaces act as effective cryopumps and are covered by several layers of molecules of the residual gas. This mechanism ensures an extremely high vacuum, as needed for the survival of cold antiprotons for hours.

During the 15 s preceding the implantation of the e^+ in the target in the \bar{H} formation experiments, the two Ps excitation lasers are fired inside the apparatus at 10 Hz. Both lasers hit a Macor screen (covered by a metallic mesh) that is mounted for diagnosis of the position and size of the lasers next to the e^+ target, in close proximity to the \bar{H}_{trap}^f . The laser pulses induce desorption⁶⁸ of the molecules

adsorbed within the area of the laser spot ($\approx 12 \text{ mm}^2$), which fly outwards from their desorption point, and hit other cold surfaces with a high probability to be re-adsorbed. However, before this re-adsorption, they temporarily increase the local density of gas in the region around the point hit by the laser, and subsequently at the position of the \bar{p} . This extra density of gas d_g can be roughly estimated as the number of extracted molecules divided by a suitable volume V_g of some cm^3 . The number $\Delta N_{\bar{p}}$ of \bar{p} annihilating in a time Δt because of the interaction with this residual gas is:

$$\Delta N_{\bar{p}} = N_{\bar{p}} \cdot d_g \cdot \sigma \cdot v_g^{\text{rel}} \cdot \Delta t \quad (9)$$

where v_g^{rel} is the relative velocity between \bar{p} and the desorbed gas and σ is the annihilation cross-section. Relation (9) shows that the laser-induced losses are proportional to the number of antiprotons, as mentioned before in the text.

Although a precise evaluation of d_g is complicated, a rough estimation of the range of the relevant quantities results in numbers compatible with the \bar{p} losses that we observe in the sample $l\bar{p}$ (of the order of one \bar{p} per μs during a time interval of few tens of μs considering the total number of cycles, as shown in the sixth column of Table 1. As a reference, assuming that the laser pulses extract almost all the gas from the surface (we can assume that we have some 10^{14} or 10^{15} adsorption sites/ cm^2 , occupied by hydrogen, nitrogen and also water⁶⁹) and that during the time between successive pulses (0.1 s), a fraction of the order of 10^{-5} of a monolayer is formed and extracted again we get $d_g \approx 10^7 \text{ cm}^{-3}$, assuming a volume V_g of few tens cm^3 . Then, with $v_g^{\text{rel}} \approx 10^4 \text{ m s}^{-1}$, $\sigma \approx 10^{-16} \text{ cm}^2$ ⁷⁰ and $N_{\bar{p}} = 1.58 \times 10^9$, $\Delta N_{\bar{p}} \approx 1$ in $1 \mu\text{s}$ is obtained.

Data availability

The data that support the plots within this paper and other findings of this study are available from the corresponding author upon reasonable request.

Code availability

The simulation and the data analysis are developed using custom codes based on publicly available frameworks: geant4 (<https://geant4.web.cern.ch/>) and ROOT (<https://root.cern/>). The codes are available from the corresponding author upon reasonable request.

Received: 29 September 2020; Accepted: 2 November 2020;

Published online: 08 February 2021

References

- Nieto, M. M. & Goldman, J. T. The arguments against antigravity and the gravitational acceleration of antimatter. *Phys. Rep.* **205**, 221–281 (1991).
- Apostolakis, A. et al., CPLEAR Collaboration. Test of the equivalence principle with neutral kaons. *Phys. Lett. B* **452**, 425–433 (1999).
- Gabrielse, G. et al. Precision mass spectroscopy of the antiproton and proton using simultaneously trapped particles. *Phys. Rev. Lett.* **82**, 3198–3201 (1999).
- Touboul, P. et al. MICROSCOPE mission: first results of a space test of the equivalence principle. *Phys. Rev. Lett.* **119**, 231101 (2017).
- Tanabashi, M. et al., Particle Data Group. The review of particle physics. *Phys. Rev. D* **98**, 030001 (2018).
- Kostelecky, V. A. & Vargas, A. J. Lorentz and CPT tests with hydrogen, antihydrogen, and related systems. *Phys. Rev. D* **92**, 056002 (2015).
- Benoit-Lévy, A. & Chardin, G. Introducing the Dirac-Milne universe. *Astron. Astrophys.* **537**, A78 (2012).
- Lueders, G. Proof of the TCP theorem. *Ann. Phys.* **2**, 1–15 (1957).
- Amoretti, M. et al., ATHENA Collaboration. Production and detection of cold antihydrogen atoms. *Nature* **419**, 456–459 (2002).
- Gabrielse, G. et al., ATRAP Collaboration. Background-free observation of cold antihydrogen with field-ionization analysis of its states. *Phys. Rev. Lett.* **89**, 213401 (2002).
- Andresen, G. B. et al. Trapped antihydrogen. *Nature* **468**, 673–676 (2010).
- Ahmadi, M. et al., ALPHA Collaboration. Observation of the 1S–2S transition in trapped antihydrogen. *Nature* **541**, 506–510 (2017).
- Ahmadi, M. et al., ALPHA Collaboration. Observation of the hyperfine spectrum of antihydrogen. *Nature* **548**, 66–69 (2017).
- Ahmadi, M. et al., ALPHA Collaboration. An improved limit on the charge of antihydrogen from stochastic acceleration. *Nature* **529**, 373–376 (2016).
- Doser, M. et al., AEGIS Collaboration. Exploring the WEP with a pulsed beam of cold antihydrogen. *Class. Quantum Grav.* **29**, 184009 (2012).

16. Charman, A. E. et al., ALPHA Collaboration. Description and first application of a new technique to measure the gravitational mass of antihydrogen. *Nat. Commun.* **4**, 1785 (2013).
17. Sacquin, Y. The GBAR experiment: gravitational behaviour of antihydrogen at rest. *Eur. Phys. J. D* **68**, 31 (2014).
18. Cassidy, D. B. Experimental progress in positronium laser physics. *Eur. Phys. J. D* **72**, 53 (2018).
19. Antognini, A. et al. Studying antimatter gravity with muonium. *Atoms* **6**, 17 (2018).
20. Amoretti, M. et al., ATHENA Collaboration. High rate production of antihydrogen. *Phys. Lett. B* **578**, 23–32 (2004).
21. Storry, C. et al., ATRAP Collaboration. First laser-controlled antihydrogen production. *Phys. Rev. Lett.* **93**, 263401 (2004).
22. Wolz, T., Malbrunot, C., Vieille-Grosjean, M. & Comparat, D. Stimulated decay and formation of antihydrogen atoms. *Phys. Rev. A* **101**, 043412 (2020).
23. Maury, S. The antiproton decelerator: AD. *Hyperfine Interact.* **109**, 43–52 (1997).
24. Aghion, S. et al., AEgIS Collaboration. A moiré deflectometer for antimatter. *Nat. Commun.* **5**, 4538 (2014).
25. Charlton, M. Antihydrogen production in collisions of antiprotons with excited states of positronium. *Phys. Lett. A* **143**, 143–146 (1990).
26. Krasnicky, D., Caravita, R., Canali, C. & Testera, G. Cross section for Rydberg antihydrogen production via charge exchange between Rydberg positroniums and antiprotons in a magnetic field. *Phys. Rev. A* **94**, 022714 (2016).
27. Krasnicky, D., Testera, G. & Zurlo, N. Comparison of classical and quantum models of anti-hydrogen formation through charge exchange. *J. Phys. B* **52**, 115202 (2019).
28. Mariazzi, S. et al. High positronium yield and emission into the vacuum from oxidized tunable nanochannels in silicon. *Phys. Rev. B* **81**, 235418 (2010).
29. Major, F. G., Gheorghe, V. N. & Werth, G. *Charged Particle Traps Springer Series on Atomic, Optical, and Plasma Physics* (Springer, Berlin, Heidelberg, 2005).
30. Dubin, D. H. E. & O’Neil, T. M. Trapped non-neutral plasmas, liquids, and crystals (the thermal equilibrium states). *Rev. Mod. Phys.* **71**, 87–172 (1999).
31. Caravita, R. et al., AEgIS Collaboration. Positronium Rydberg excitation diagnostic in a 1T cryogenic environment. *AIP Conf. Proc.* **2182**, 030002 (2019).
32. Antonello, M. et al., AEgIS Collaboration. Rydberg-positronium velocity and self-ionization studies in 1T magnetic field and cryogenic environment. *Phys. Rev. A* **102**, 013101 (2020).
33. Aghion, S. et al., AEgIS Collaboration. Laser excitation of the $n = 3$ level of positronium for antihydrogen production. *Phys. Rev. A* **94**, 012507 (2016).
34. Aghion, S. et al., AEgIS Collaboration. Compression of a mixed antiproton and electron non-neutral plasma to high densities. *Eur. Phys. J. D* **72**, 76–86 (2018).
35. Andresen, G. B. et al., ALPHA Collaboration. Compression of antiproton clouds for antihydrogen trapping. *Phys. Rev. Lett.* **100**, 203401 (2008).
36. Kuroda, N. Radial compression of an antiproton cloud for production of intense antiproton beams. *Phys. Rev. Lett.* **100**, 203402 (2008).
37. Spencer, R. L., Rasband, S. N. & Vanfleet, R. R. Numerical calculation of axisymmetric non-neutral plasma equilibria. *Phys. Fluids B* **5**, 4267–4272 (1993).
38. Eggleston, D. L. et al. Parallel energy analyzer for pure electron plasma devices. *Phys. Fluids B* **4**, 3432–3439 (1992).
39. Nagashima, Y. et al. Origin of positronium emitted from SiO₂. *Phys. Rev. B* **58**, 12676–12679 (1998).
40. Zurlo, N. et al., AEgIS Collaboration. Calibration and equalisation of plastic scintillator detector for antiproton annihilation identification over positron/positronium background. *Acta Phys. Pol. B* **51**, 213–223 (2020).
41. Agostinelli, S. et al. Geant4, a simulation toolkit. *Nucl. Instrum. Meth. A* **506**, 250–303 (2003).
42. Kohlhoff, M. W. Interaction of Rydberg atoms with surfaces. *Eur. Phys. J. Spec. Top.* **225**, 3061–3085 (2016).
43. Puska, M. J. et al. Positrons affinities for elemental metals. *J. Phys. Condens. Matter* **1**, 6081–6094 (1989).
44. Sekatskii, S. K. On the reflection of Rydberg atoms from a liquid helium surface. *Z. Phys. D* **35**, 225–229 (1995).
45. Storey, J. et al., AEgIS Collaboration. Particle tracking at 4 K: the Fast Annihilation Cryogenic Tracking (FACT) detector for the AEgIS antimatter gravity experiment. *Nucl. Instrum. Meth. A* **732**, 437–441 (2013).
46. Amsler, C. et al., AEgIS Collaboration. A cryogenic tracking detector for antihydrogen detection in the AEgIS experiment. *Nucl. Instrum. Meth. A* **960**, 163637 (2020).
47. Cerchiari, G., Yzombard, P. & Kellerbauer, A. Laser-assisted evaporative cooling of anions. *Phys. Rev. Lett.* **123**, 103201 (2019).
48. Tang, R. et al. Candidate for laser cooling of a negative ion: high-resolution photoelectron imaging of Th⁻. *Phys. Rev. Lett.* **123**, 203002 (2019).
49. Gerber, S., Fesel, J., Doser, M. & Comparat, D. Photodetachment and Doppler laser cooling of anionic molecules. *N. J. Phys.* **20**, 023024 (2018).
50. ALPHA Collaboration. Spectroscopic and gravitational measurements on antihydrogen: ALPHA-3, ALPHA-g and beyond. <http://cds.cern.ch/record/2691557/files/SPSC-P-362.pdf> (2019).
51. Drobyshev, G. et al. Proposal for the AEGIS experiment at the CERN antiproton decelerator (Antimatter Experiment: Gravity, Interferometry, Spectroscopy). <https://cds.cern.ch/record/1037532/files/spsc-2007-017.pdf> (2007).
52. Kuroda, N. et al. A source of antihydrogen for in-flight hyperfine spectroscopy. *Nat. Commun.* **5**, 3089 (2014).
53. Malbrunot, C. et al. The ASACUSA antihydrogen and hydrogen program: results and prospects. *Philos. Trans. R. Soc. A* **376**, 2116 (2018).
54. Comparat, D. & Malbrunot, C. Laser-stimulated de-excitation of Rydberg antihydrogen atoms. *Phys. Rev. A* **99**, 013418 (2019).
55. Diermaier, M. et al. In-beam measurement of the hydrogen hyperfine splitting and prospects for antihydrogen spectroscopy. *Nat. Commun.* **8**, 15749 (2017).
56. Testera, G. et al., AEgIS Collaboration. Formation of a cold antihydrogen beam in AEGIS for gravity measurements. *AIP Conf. Proc.* **1037**, 5–15 (2008).
57. Hogan, S. D. Rydberg-Stark deceleration of atoms and molecules. *EPJ Techn. Instrum.* **3**, 2–52 (2016).
58. Maury, S. et al. ELENA: the extra low energy anti-proton facility at CERN. *Hyperfine Interact.* **229**, 105–115 (2014).
59. Amsler, C. et al., AEgIS Collaboration. A $\approx 100 \mu\text{m}$ resolution position-sensitive detector for slow positronium. *Nucl. Instrum. Meth. B* **457**, 44–48 (2019).
60. Gabrielse, G. et al. First capture of antiprotons in a Penning trap: a kiloelectronvolt source. *Phys. Rev. Lett.* **57**, 2504–2507 (1986).
61. Fani, M. et al., AEgIS Collaboration. Developments for pulsed antihydrogen production towards direct gravitational measurement on antimatter. *Phys. Scr.* **95**, 114001 (2020).
62. Aghion, S. et al., AEgIS Collaboration. Positron bunching and electrostatic transport system for the production and emission of dense positronium clouds into vacuum. *Nucl. Instrum. Meth. B* **362**, 86–92 (2015).
63. Danielson, J. R., Dubin, D. H. E., Greaves, R. G. & Surko, C. Plasma and trapped techniques for science with positrons. *Rev. Mod. Phys.* **87**, 247–306 (2015).
64. Cassidy, D. B., Deng, S. H. M., Tanaka, H. K. M. & Mills, A. P. Jr Single shot positron annihilation lifetime spectroscopy. *Appl. Phys. Lett.* **88**, 194105 (2006).
65. Castelli, F. et al. Efficient positronium laser excitation for antihydrogen production in a magnetic field. *Phys. Rev. A* **78**, 052512 (2008).
66. Alonso, A. M. et al. State-selective electric-field ionization of Rydberg positronium. *Phys. Rev. A* **98**, 053417 (2018).
67. Zurlo, N. et al., AEgIS Collaboration. Monte-Carlo simulation of positronium laser excitation and anti-hydrogen formation via charge exchange. *Hyperfine Interact.* **240**, 18–28 (2019).
68. Sneh, O., Cameron, M. A. & George, S. M. Adsorption and desorption kinetics of H₂ on a fully hydroxylated SiO₂ surface. *Surf. Sci.* **364**, 61–78 (1996).
69. Jousten, K. *Handbook of Vacuum Technology* (Wiley-VCH, 2016).
70. Cohen, J. Capture of antiprotons by some radioactive atoms and ions. *Phys. Rev. A* **69**, 022501 (2004).

Acknowledgements

We would like to acknowledge and thank Dr Michele Sacerdoti for his useful work within the collaboration since the beginning and for his further Monte Carlo simulations. Similarly, we thank Lillian Smestad and Giovanni Cerchiari for their contributions to the preparatory work that resulted in this paper. This work has been performed in the framework of the AEgIS Collaboration and it was supported by Istituto Nazionale di Fisica Nucleare (INFN-Italy); the CERN Fellowship and Doctoral student programs; the Swiss National Science Foundation Ambizione Grant No. 154833; a Deutsche Forschungsgemeinschaft research grant; an excellence initiative of Heidelberg University; Marie Skłodowska-Curie Innovative Training Network Fellowship of the European Commission Horizon 2020 Program No. 721559 AVA; European’s Research Council under the European Unions Seventh Framework Program FP7/2007–2013 Grants Nos. 291242 and 277762; European’s Union Horizon 2020 research and innovation program under the Marie Skłodowska-Curie grant agreements ANGRAM No. 748826; No. 754496, FELLINI, and No. 665779, COFUND-FP-CERN-2014; Austrian Ministry for Science, Research, and Economy; Research Council of Norway; Bergen Research Foundation; John Templeton Foundation; Institut de Physique Nucleaire et des Particules and Institut National de Physique (France); Ministry of Education and Science of the Russian Federation and Russian Academy of Sciences and the European Social Fund within the framework of realizing research infrastructure for experiments at CERN, LM2015058; Big-Open Data Innovation Laboratory (BODaI-Lab), University of Brescia, granted by Fondazione Cariplo and Regione Lombardia (Italy).

Author contributions

All authors have contributed to this publication, being variously involved in the design and construction of the detectors, writing software, calibrating sub-systems, operating the detectors, acquiring data, and analyzing the processed data.

Competing interests

The authors declare no competing interests.

Additional information

Correspondence and requests for materials should be addressed to G.T.

Reprints and permission information is available at <http://www.nature.com/reprints>

Publisher's note Springer Nature remains neutral with regard to jurisdictional claims in published maps and institutional affiliations.



Open Access This article is licensed under a Creative Commons Attribution 4.0 International License, which permits use, sharing, adaptation, distribution and reproduction in any medium or format, as long as you give appropriate credit to the original author(s) and the source, provide a link to the Creative Commons license, and indicate if changes were made. The images or other third party material in this article are included in the article's Creative Commons license, unless indicated otherwise in a credit line to the material. If material is not included in the article's Creative Commons license and your intended use is not permitted by statutory regulation or exceeds the permitted use, you will need to obtain permission directly from the copyright holder. To view a copy of this license, visit <http://creativecommons.org/licenses/by/4.0/>.

© The Author(s) 2021

¹Stefan Meyer Institute for Subatomic Physics, Austrian Academy of Sciences, Boltzmannngasse 3, 1090 Vienna, Austria. ²Department of Science, University of Insubria, Via Valleggio 11, 22100 Como, Italy. ³INFN Milano, via Celoria 16, 20133 Milano, Italy. ⁴Institute for Nuclear Research of the Russian Academy of Science, Moscow 117312, Russia. ⁵Department of Mechanical and Industrial Engineering, University of Brescia, via Branze 38, 25123 Brescia, Italy. ⁶INFN Pavia, via Bassi 6, 27100 Pavia, Italy. ⁷Department of Physics, Univ. of Trento, via Sommarive 14, 38123 Povo, Trento, Italy. ⁸TIFPA/INFN Trento, via Sommarive 14, 38123 Povo, Trento, Italy. ⁹Physics Department, CERN, 1211 Geneva, Switzerland. ¹⁰Department of Physics 'Aldo Pontremoli', Univ. of Milano, via Celoria 16, 20133 Milano, Italy. ¹¹Laboratoire Aimé Cotton, Univ. Paris-Sud, ENS Paris Saclay, CNRS, Univ. Paris-Saclay, 91405 Orsay, France. ¹²Department of Aerospace Science and Technology, Politecnico di Milano, via La Masa 34, 20156 Milano, Italy. ¹³Kirchhoff Institute for Physics, Heidelberg Univ., Im Neuenheimer Feld 227, 69120 Heidelberg, Germany. ¹⁴Department of Physics, Univ. of Genova, via Dodecaneso 33, 16146 Genova, Italy. ¹⁵INFN Genova, via Dodecaneso 33, 16146 Genova, Italy. ¹⁶LNESS, Department of Physics, Politecnico di Milano, via Anzani 42, 22100 Como, Italy. ¹⁷Max Planck Institute for Nuclear Physics, Saupfercheckweg 1, 69117 Heidelberg, Germany. ¹⁸INFN Padova, via Marzolo 8, 35131 Padova, Italy. ¹⁹Univ Lyon, Univ. Claude Bernard Lyon 1, CNRS/IN2P3, IP2I Lyon, 69622 Villeurbanne, France. ²⁰Czech Technical University, Břehová 7, 11519 Prague, Czech Republic. ²¹Univ. of Bologna, Viale Berti Pichat 6/2, 40126 Bologna, Italy. ²²Department of Physics, Univ. of Oslo, Sem Sælandsvei 24, 0371 Oslo, Norway. ²³Department of Physics, Univ. of Pavia, via Bassi 6, 27100 Pavia, Italy. ²⁴Department of Physics, Heidelberg Univ., Im Neuenheimer Feld 226, 69120 Heidelberg, Germany. ²⁵Department of Civil, Environmental, Architectural Engineering and Mathematics, Univ. of Brescia, via Branze 43, 25123 Brescia, Italy. ²⁶Present address: Kastler Brossel Lab., Sorbonne Univ., CNRS, ENS Univ. PSL, Collège de France, 4 Place Jussieu, case 74, 75252 Paris, France. [✉]email: testera@ge.infn.it